Doped silicon nanoparticles for enhanced charge transportation in organic-inorganic hybrid solar cells

Hemaprabha Elangovan[a], Upendra K. Pandey[a], Kamanio Chattopadhyay[a,b], Praveen C Ramamurthy[a,b,*]

[a]Interdisciplinary Centre for Energy Research, Indian Institute of Science, Bangalore 560012, India

[b]Department of Materials Engineering, Indian Institute of Science, Bangalore 560012, India

E-mail: hemazephyrs@gmail.com, upendrap@iisc.ac.in, kamanioc@iisc.ac.in, praveen@iisc.ac.in

Abstract

In this work, we have added p-type and n-type Si nanoparticles (NPs) obtained from cryomilling, in poly(3-hexylthiophene) (P3HT) and [6,6]-phenyl-C61-butyric acid methyl ester ($PC_{61}BM$) organic photovoltaic cell at different weight ratios and their effect on organic-inorganic hybrid solar cell device parameters has been evaluated. It is observed that the addition of p-type nanoparticles tailors the energy band alignment at the P3HT/NP interface which provides efficient charge carrier transport enhancing the photo-conversion efficiency by more than 21%. Enhancement is reflected by an improvement in short-circuit current by ~35% with respect to reference P3HT:$PC_{61}BM$ device without Si NPs. However, for n-type NPs where the optimum cascading band alignment does not occur, only 10% improvement in photo-conversion efficiency is observed. This work insight how performance of organic solar cells can be tailored by size factor as well as energy level tuning of the added nanoparticles.

Keywords: Hybrid solar cell; silicon nanoparticle; energy level alignment; exciton dissociation.

1. Introduction

Bulk heterojunction solar cells have the blend of acceptor and donor materials with domain size in the range of few nanometres, as active absorption layer. The first bulk heterojunction solar cell was successfully fabricated by Yu G. et al., in the year 1995 and the photo conversion efficiency (PCE) of about 1% was shown (Yu et al., 1995). The studies were then focused to improve the PCE by tuning certain parameters such as absorbance of the donor material by mixing energy band-engineered polymers to broaden the absorption band-width (Yang et al., 2015), optical properties of the blend (Zhu et al., 2012), optimizing the domain formation and size (A. Dowland et al., 2013; MacLachlan et al., 2015) and engineering the interfacial area (Pfadler et al., 2014; Yin et al., 2016). One of such approaches was to introduce inorganic semiconductor particles in the active material, which resulted in the advent of hybrid solar cells (Zhou et al., 2010). Utilization of several inorganic particles such as CdTe (Gur et al., 2006), CdS (Lee et al., 2008; Wang et al., 2007), CdSe (Yang et al., 2011; Zhou et al., 2011a), ZnO (Hames et al., 2010; Takanezawa et al., 2008; Venkataprasad Bhat et al., 2011), TiO_2 (Kuo et al., 2008), PbS (Tsang et al., 2009), PbSe (Tan et al., 2009), SnO_2 (Kudo et al., 2007), $CuInS_2$ (Arici et al., 2003) have been reported. These particles were primarily in alloy or compound form and they were also introduced as core-shell structures (Jaramillo et al., 2015).

In hybrid solar cells, the first utilization of elementary nanoparticle-silicon was explored by Liu C. Y. et al., by incorporating Si nanoparticles (NPs) in poly-3(hexylthiophene) and has shown a maximum photo-conversion efficiency of 1.15% (Liu et al., 2009). Over the subsequent years, further optimization of the processing parameters of active material, and electrode selection have resulted in maximum efficiency of 1.47% (Liu et al., 2010). Recently, Shuangyi Z. et. al., has shown an improvement in efficiency of poly(3-hexylthiophene) (P3HT):[6,6]-phenyl-C61-butyric acid methyl ester ($PC_{61}BM$) solar cells, by incorporating Si NPs and obtaining a cascade band structure (Zhao et al., 2016). Dayal S. et. al., has reported previously by addition of the inorganic nanoparticles enhances PCE by improving the optical absorption of active material as well as simultaneously providing an efficient pathway for the generated charge carriers (Dayal et al., 2010). The pathway can be tuned by utilizing the NPs with various transport energy levels for different polymer blends. However, the change in energy level is mainly achieved by reducing the particle size to the range of quantum confinement (Dayal et al., 2010; Zhou et al., 2011b).

In addition to size reduction, doping is also one of the effective ways to fine tune the energy levels of semiconducting nanoparticles (Streetman and Banerjee, 2015). Therefore, to understand the utilization of doped NPs in hybrid solar cells, silicon particles with various dopant (n-type and p-type) have been

synthesized and subsequently used with active material. The reference with various material was P3HT and $PC_{61}BM$ because this material blend continues to be the choice for fundamental studies in hybrid solar cells (Chi et al., 2014). In this study, n-type and p-type Si NPs having tailored energy levels are added with P3HT:$PC_{61}BM$ in various weight percentage and their effect on solar cell parameters have been investigated. The phenomenon of tuning the charge carrier states by the deployment of the dopant levels in Si NPs have also been discussed in subsequent sections.

2. Experimental Details

2.1 Synthesis of Silicon Nanoparticles

To obtain n-type Si NPs, phosphorous doped silicon wafer with 1-10 Ω-cm resistivity was used, while for p-type Si NPs, boron doped silicon wafer with same resistivity was used. The silicon wafers were broken into small pieces and milled to obtain the respective doped Si NPs. The Si NPs obtained from cryomilling (Barai et al., 2012) were used for device fabrication. These particles were dispersed in ethanol and sonicated for 15 min. This solution was then centrifuged at 10000 rpm and the homogeneous sized particles were collected. These particles were etched with 2 vol% hydrofluoric acid (HF) to get rid of oxide layer and the resulting particles were dispersed in iso-propyl alcohol (IPA).

2.2 Device Fabrication

Before active layer deposition, the ITO-coated patterned glass substrates of ~15 ohm/cm^2, (Xinyan Technology Limited, Taiwan) were cleaned using ultrasonicator bath in the following sequence – DI water with soap solution (Hellmanex III, 3% in DI water), DI water, IPA and acetone. Substrates were then dried using nitrogen gas before being placed inside UV ozone cleaner for UV ozone treatment to remove residual impurities. The electron transporting layer ZnO was spin coated from di-ethyl zinc solution (DEZ), (15% in toluene (Aldrich)), solution prepared from mixing DEZ with tetrahydrofuran in 1:6 (vol/vol) inside glove box on cleaned ITO substrate. ZnO coated substrates were than annealed at 130° C for 20 minutes in ambient with humidity less than 35% RH, resulting ~30 nm thick film. ZnO coated samples were then immediately transferred inside the glove box (Jacomax, O_2 < 5 ppm, H_2O < 5 ppm) for further processing. The active material blend of P3HT and $PC_{61}BM$ was prepared in chlorobenzene (1:0.8 by wt. %) and kept for stirring at 60 °C overnight. The Si nanoparticles were etched with hydrofluoric acid (2 vol%), in order to avoid oxidation of the particles and were dispersed in IPA (2 mg/ml). Si nanoparticles dispersed in IPA was then taken inside the glove box and were continuously stirred before being taken in different vials for

different weight ratios. Subsequently IPA was evaporated from the Si NPs dispersion before P3HT:$PC_{61}BM$ was added. The solution was again stirred for another 30 min before being used for device fabrication to make sure the uniform distribution of the NPs in the active layer. Finally, devices were fabricated with different weight ratios (0.5,1.3, 2.6, 3.9, 7.8) of n-type and p-type Si NPs with P3HT:$PC_{61}BM$ blends using spin coating. The samples are named as, 'p0.5, p1.3, p2.6, p3.9 and p7.8' for p-type Si NPs incorporated devices at various weight ratios. Similarly, n-type Si NPs incorporated devices are named as 'n0.5, n1.3, n2.6, n3.9, n7.8'. Sample without NP incorporation is considered as the Reference device and named as 'Ref'. Active layer was spin coated on ZnO layer for 60 seconds at 1000 rpm (thickness of about 120 nm) and then annealed at 140° C for 15 minutes. Finally, top contact of MoO_3 and Ag with a thickness of 10 nm and 120 nm respectively was evaporated at a base pressure of 3.6×10^{-6} mbar in order to complete the device. The active area of the device was 9 mm^2, calculated with the overlap area of top and bottom contact.

2.3 Measurement

X-ray diffraction (XRD) studies were performed by subjecting the powder to Cu Kα (λ = 0.15402 nm) radiation in the 2θ range of 10° to 80°. Transmission electron microscopy (TEM) study was performed using Tecnai T20 microscope at 200 kV equipped with LaB6 emissions gun. TEM samples were prepared by drop-casting the Si dispersion on carbon-coated copper grids and used after solvent evaporation. Diffused reflectance spectroscopy (DRS) measurements were carried out using a Perkin Elmer UV-Vis-Near IR spectrometer. The photoluminescence studies were carried out in Perkin Elmer fluorescence spectrophotometer. The current density–voltage (*J–V*) were measured using a Keithley 4200 parameter analyzer and incident light intensity of 100 mW/cm^2 using Oriel Sol3A Class AAA solar simulator (intensity was calibrated for 1 sun using NREL certified Si detector with KG5 filter). External quantum efficiency (EQE) was measured using an Enlitech setup (model QE-R). Both device fabrication and characterization has been carried out using Jacomex glove box integrated with Angstrom Engineering thermal evaporator, solar simulator and EQE set-up. Nanosurf easyscan2 atomic force microscope (AFM) was used to study the morphology of the active layer.

3. Results and Discussions

3.1 Structural and Optical Properties of cryomilled Silicon

Si NPs were synthesized by cryomilling the silicon wafers for 10 hours (Barai et al., 2012) and the structural characterization of the obtained NPs is provided in Fig. 1. The milled powder was subjected to the XRD

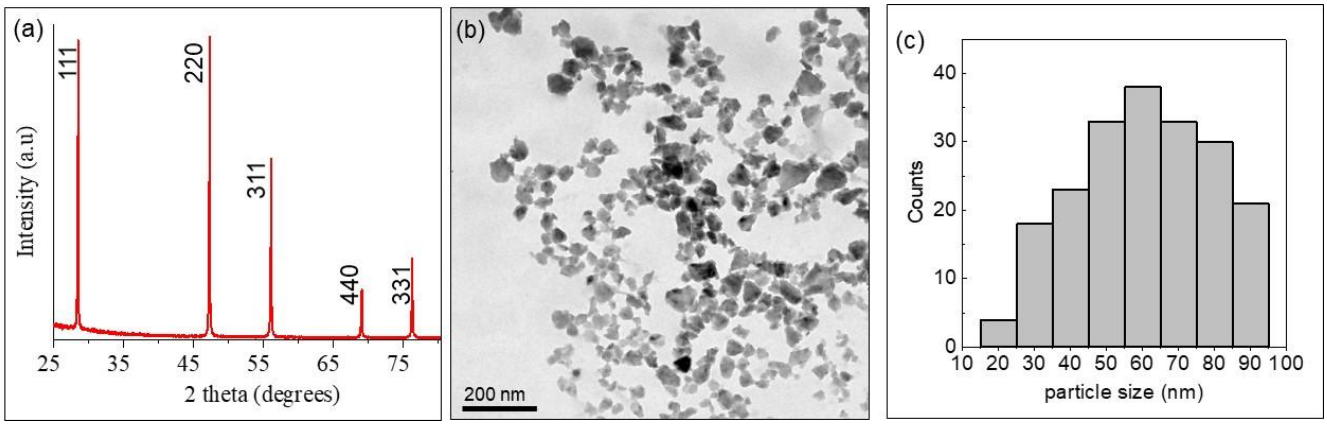

Fig. 1. Structural characterization of Si NPs. a) XRD pattern indexed to silicon diamond cubic structure. b) TEM bright-field image showing the distribution of Si NPs and c) Particle size distribution of the sample computed using the TEM images from different regions, having a peak at 60 nm.

analysis which suggests the Si diamond cubic structure as shown in Fig. 1a. The milled powder was centrifuged in order to get rid of larger particles. TEM bright-field images show distribution of nano-sized particles obtained (Fig. 1b). The distribution of the nanoparticles obtained from these images are shown in Fig. 1c. The particle size varies from 20 nm to 90 nm with mode at 60 nm.

Both the p-type and n-type wafers were subjected to milling to obtain nanoparticles. The Si NPs obtained from p-type wafer will be referred as 'pSi NPs', while those obtained from n-type wafer will be referred as 'nSi NPs'.

Diffused reflectance spectroscopy of the pSi and nSi NPs recorded in the wavelength range of 200-2000 nm are shown in Fig. 2a. Based on the percent reflectance values obtained from the DRS measurement, Tauc plot has been obtained and is shown in Fig. 2b.

Silicon exhibits wide range of light absorption and is an indirect bandgap material. Bohr radius of silicon is 5 nm and the silicon nanoparticles can exhibit direct transition when quantum confinement range is reached (Naoto et al., 2010; Wilcoxon et al., 1999). In this work, have not reached the size of particle is 20 – 90 nm (Fig. 1c). Hence, the Tauc plot exponent for indirect band gap is used in band gap calculations. The band gap of the Si NPs obtained was calculated using the Tauc plot (Tauc, 1968) and the details are given here. The amount of diffuse reflectance (R_∞) from the infinitely thick sample is provided as follows by the Kubelka Function (Kubelka, 1948), in Eqn. 1 :

(1)

where A is the absorption coefficient and S is the scattering coefficient of the material (Kundu and Varma, 2013).

Eqn. 2 provides the Tauc relation for indirect bandgap materials, where α is the absorption coefficient, E_g is the optical bandgap of the material.

(2)

Correlating the absorption coefficient in Eqns. 1 and 2 considering the scattering coefficient remains

(3)

unchanged with the wavelength of the light, Tauc relation can be expressed as given in Eqn. 3.

Fig. 2b and 2c. show the Tauc plots obtained using the relationship in Eqn. 3, and the bandgap for pSi and nSi particles are obtained by extrapolating the linear portion of the curve to the X-axis (eV). The bandgap value estimated for both pSi NPs and nSi NPs is 1.09 eV.

Fermi levels of the silicon NPs can change due to doping and the fermi level values were calculated using the following equations [25]:

(4.1)

(4.2)

where E_f (p) – Fermi level of the pSi NPs, E_f (n) – Fermi level of the nSi NPs, E_i – Fermi level of the intrinsic silicon, k – Boltzmann Constant, T – Working Temperature, n_i is the intrinsic carrier concentration of

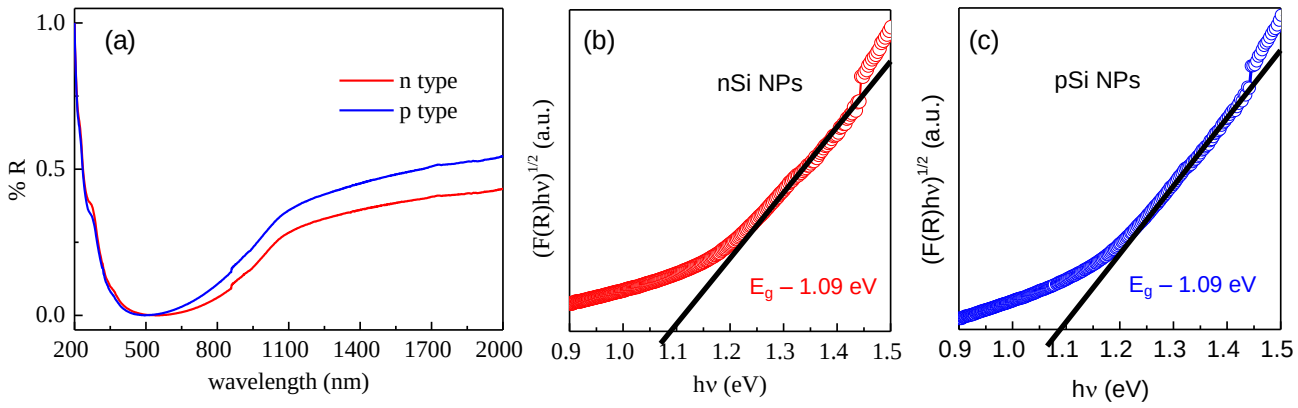

Fig. 2. a) Diffused reflectance spectra of pSi and nSi NPs synthesized by cryomilling. b) Tauc plot for nSi NPs showing the bandgap at 1.09 eV and c) Tauc plot for pSi NPs showing the bandgap at 1.09 eV.

silicon, n, p – Carrier concentration of n-type and p-type silicon respectively. Calculated Fermi levels of the doped wafers are listed in the Table I.

Table I
Parameters used in the calculation of Fermi levels of nSi and pSi NPs and the results obtained

		Values	Unit
E_i	Intrinsic Fermi Level	4.60	eV
n	Electron concentration	1.3E15 - 1.5E16	cm^{-3}
p	Hole concentration	1.4E15 - 1.4E16	cm^{-3}
$E_f(p)$	Fermi level in pSi NPs	4.93 eV	eV
$E_f(n)$	Fermi level in nSi NPs	4.30 eV	eV

3.2 Device Performance

In order to avoid the oxidation layer formed in NPs, the Si NPs were etched with HF and subsequently used in device fabrication.

J-V curves under 100 mW/cm^2 illumination for the reference device, pSi NPs and nSi NPs incorporated

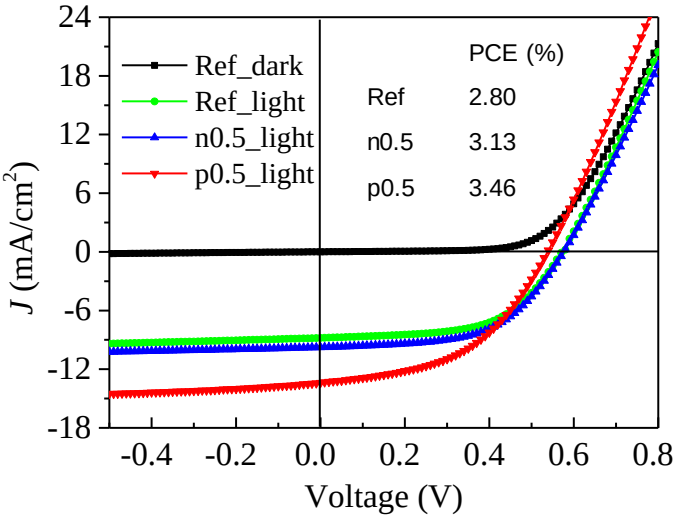

Fig. 3. *J-V* curves for the reference, nSi and pSi NPs incorporated devices and their photo-conversion efficiency.

devices are shown in Fig. 3. Short-circuit current (J_{SC}) value of reference cell is 8.65 mA/cm^2. *J-V* curves show that the J_{SC} increases to 13.39 mA/cm^2 during the addition of pSi NPs, while that increases to 9.73 mA/cm^2 during the addition of nSi NPs. Device efficiency is observed to increase with the addition of both p-type and n-type Si NPs to 3.46% and 3.13% respectively. Addition of NPs, helps in exciton dissociation and charge carrier transport. Charge transport in organic material occur by hoping mechanism and these NPs, helps in connecting domains for charge to move easily. This enhances the current collection, which reflects in improvement of J_{SC} (Wright and Uddin, 2012). To probe the origin of the parameters resulting in the enhancement of device efficiency, energy band structures of the devices are given in Fig. 4a and Fig. 4b. Work function of the various layers used in the device is given in Table II.

Table II
Work function of the various layers used in the device structure and their nomenclature

$E_{cathode}$	work function of e^- collector (ITO)	4.60 eV
E_{anode}	work function of h^+ collector (Al)	4.30 eV
E_{ETL}	work function of e^- transport layer (ZnO)	4.20 eV
E_{HTL}	work function of h^+ transport layer (MoO_3)	5.20 eV

$VB_{(P3HT)}$	HOMO level of P3HT	5.30 eV
$CB_{(P3HT)}$	LUMO level of P3HT	2.90 eV
$VB_{(PCBM)}$	HOMO level of $PC_{61}BM$	6.10 eV
$CB_{(PCBM)}$	LUMO level of $PC_{61}BM$	3.80 eV
$E_f(p)$	Fermi level of pSi NPs	4.93 eV
$E_f(n)$	Fermi level of nSi NPs	4.30 eV
CB_{Si}	Conduction Band level of Si	4.05 eV
VB_{Si}	Valence Band level of Si	5.17 eV

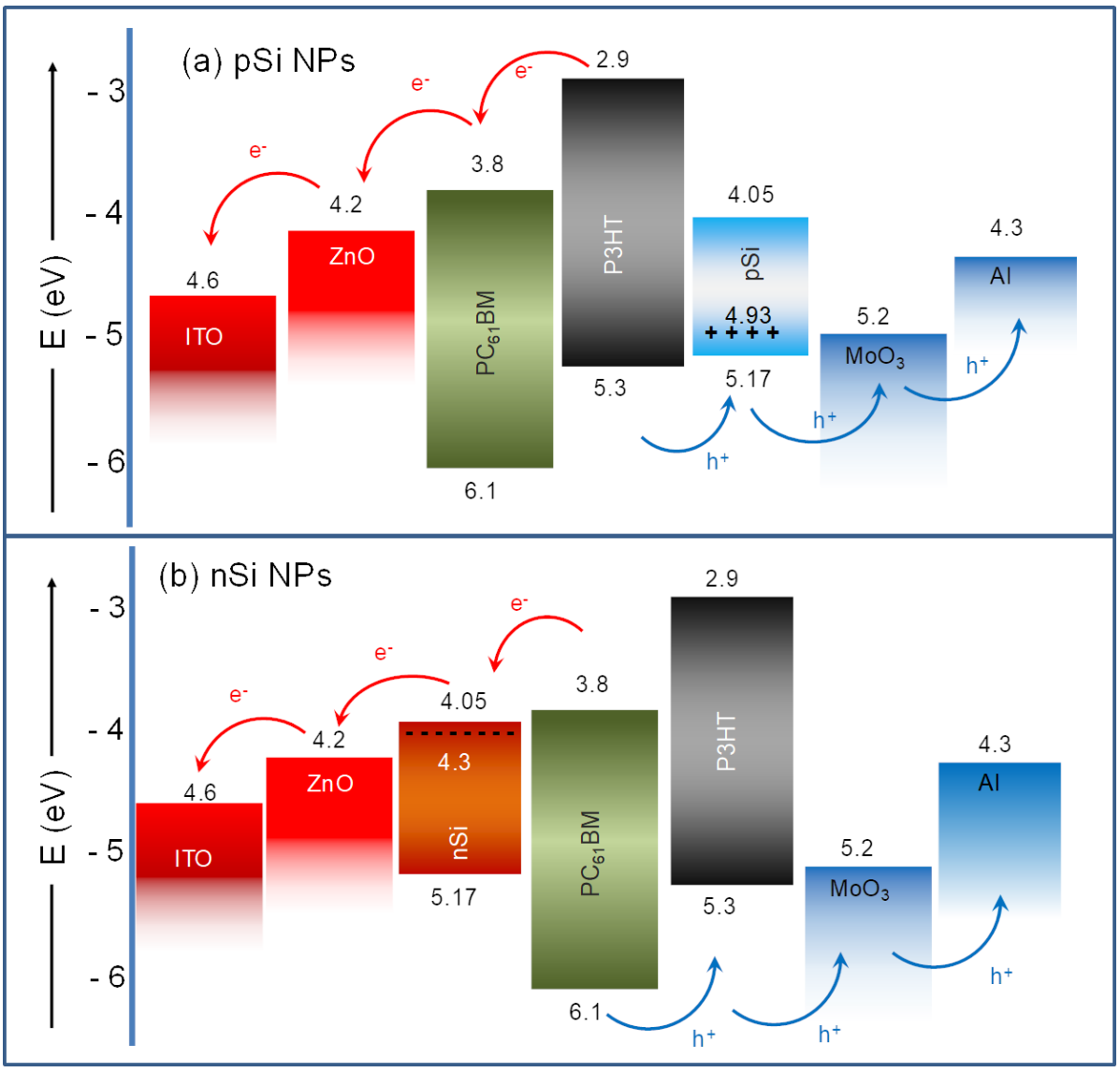

Fig. 4. Energy band alignment of the P3HT:$PC_{61}BM$ devices with a) pSi NPs and b) nSi NPs.

3.2.1. Exciton dissociation and charge carrier transport

In P3HT:$PC_{61}BM$ devices, P3HT is more efficient absorber of the incoming light than $PC_{61}BM$ (Dang et al., 2011). The absorbed light by P3HT domains generate excitons termed as Frenkel excitons (Zhu et al., 2009). The LUMO level of $PC_{61}BM$ ($CB_{(PCBM)}$) is lower than the HOMO level of P3HT ($VB_{(P3HT)}$), as can be seen in the Fig. 5. Hence, the generated relax to $PC_{61}BM$ in charge-transfer (CT) exciton state. Photo-conversion occurs after these excitons get dissociated into holes and electrons and this process requires higher energy than the binding energy between holes and electrons. These excitons will be dissociated into free charge carriers, due to the 'vibrational energy also referred as phonons' released during the relaxation process of Frenkel excitons (Narayan and Singh, 2014; Zhu et al., 2009). This process is shown schematically in Fig. 5. For inorganic materials, this binding energy will be of the order of few meV and will be provided by the thermal energy at room temperature (kT~ 0.026 eV). However, the binding energy value is three orders higher in case of organic solar cells and the general values are in the range of 0.3 eV to 1 eV (Baranovskii et al., 2012). This energy will be provided by the difference in the energy levels of the donor (P3HT) and acceptor material ($PC_{61}BM$). When Si NPs are blended with P3HT:$PC_{61}BM$, they are dispersed throughout the film as well as at interface of P3HT and $PC_{61}BM$ in active layer. Since P3HT is the

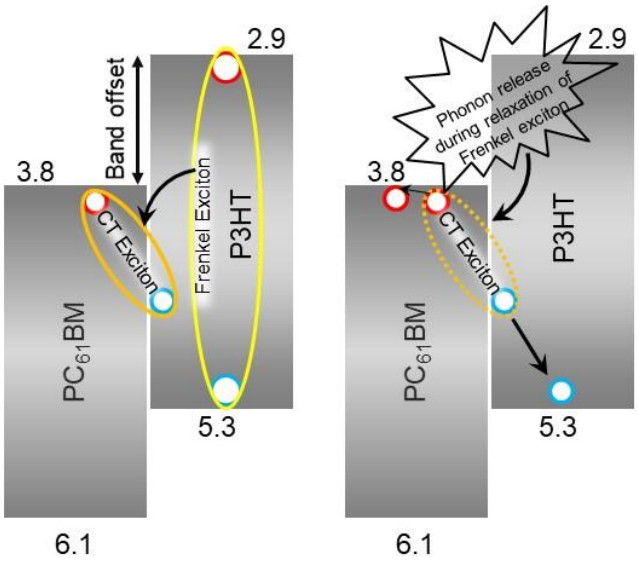

Fig. 5. Schematic showing the relaxation of Frenkel exciton and subsequent dissociation of charge-transfer exciton at the interface (Red circles represent the electrons and blue circles represent holes).

efficient absorber, exciton dissociation will also occur at P3HT/NP interface apart from P3HT:$PC_{61}BM$ interface.

For nSi NPs incorporated devices, the energy level differences between $CB_{(P3HT)}$ and CB_{Si} is 1.15 eV and this energy value is adequate to provide the energy required for exciton dissociation. Hence, the P3HT/nSi NP interface can help in exciton dissociation. These dissociated electrons will also travel from nSi NPs energy level towards the electron transport layer and subsequently collected through the respective electrode.

Addition of pSi NPs has increased PCE than nSi NP, as shown in Fig. 3. In pSi NP devices, it can be seen that the energy levels favor the exciton dissociation at the P3HT/NP interface. In the reference cell, for hole conduction the energy band alignment between the HOMO level of P3HT and the anode is important and the energy difference between $CB_{(P3HT)}$ and E_{anode} is 1 eV. In pSi device, the difference between the $VB_{(P3HT)}$ and E_f (p) is 0.37 eV and this acts as intermediate level, providing an alternate pathway for the efficient hole transport towards the anode. This additional pathway thus plays a major role in charge collection and is reflected in the *J-V* curve as shown in Fig. 4, where the J_{SC} value increases about 35% with respect to the reference device.

3.2.2. Charge transport layers

For the effective hole transportation in the device structure, MoO_3 layer has been provided. MoO_3 layer allows hole tunneling when the thickness of the layer is less than 12 nm (Cheng et al., 2011). In this work, 10 nm MoO_3 layer has been used and hence holes will tunnel through MoO_3. Additionally, the energy difference among E_{anode}, E_{HTL} and E_f (p) are considered in pSi NPs incorporated device. The energy barrier between the hole transport layer and the hole collector is 0.9 eV ($E_{anode} - E_{HTL}$). With the addition of pSi NPs, the energy barrier is reduced to 0.6 eV ($E_{anode} - E_f$ (p)). This decrease in the energy barrier of about 0.3 eV can help the device for better charge collection leading to improved photovoltaic performance parameters.

In this context, the electron transport has been enhanced in the reference structure due to the addition of ZnO. This layer is of ~30 nm thickness and tunneling of electrons through this layer is not expected. Hence, the additional interface for charge carrier transport is not available for current collection in nSi incorporated devices, showing poor increment in J_{SC} values than pSi NPs incorporated devices.

The improved current collection has been further confirmed from the improved PL quenching of the devices after the incorporation of NPs of either type specifically at lower concentrations, as shown in Fig.

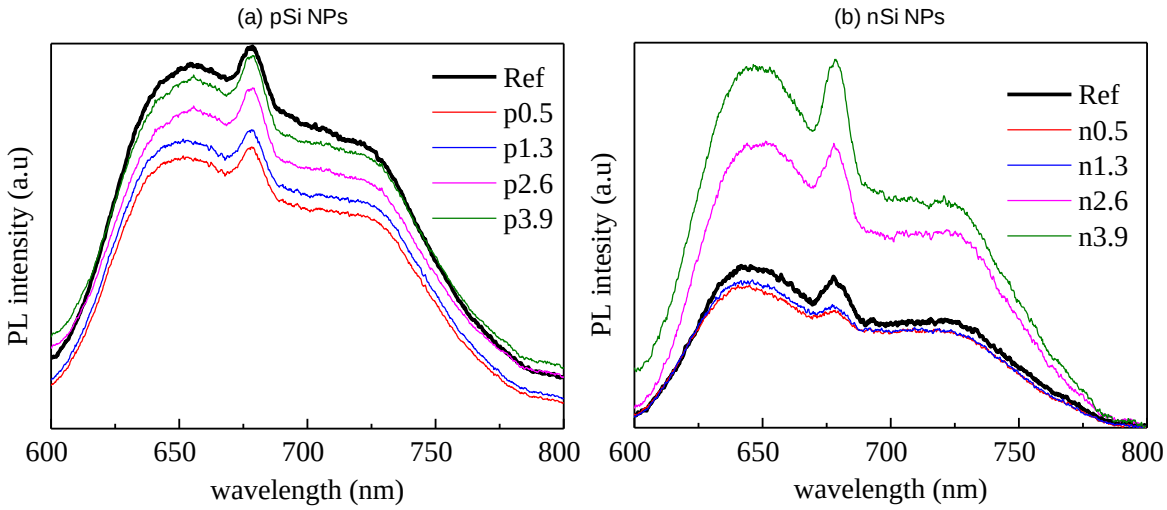

Fig. 6. Photoluminescence spectra of the active layer of devices with a) pSi NPs and b) nSi NPs.

6. PL quenching efficiency relates the amount of charge transferred from host material (P3HT) to the incorporated material (NP or PCBM in our case). It has been observed that the incorporation of pSi NPs has resulted in enhanced quenching for all the concentrations which has reflected in increased J_{SC}. However, the nSi NPs showed enhanced quenching only at low concentration and at high concentration PL quenching efficiency was reduced. Therefore, OPV devices with pSi NPs showed higher short-circuit current for all concentrations compared to nSi NPs, where the current collection takes place only at low concentrations. Next section discusses the effect of NP concentration on device performance.

3.2.3. Effect of Si NP concentration on PCE

The common trend observed during both the NPs incorporation in P3HT:$PC_{61}BM$ devices is that, efficiency increases when the NPs concentration is low and decreases with higher concentrations. Fig. 7a and 7b shows the *J-V* curve for various concentrations of pSi NPs and nSi NPs that are incorporated into the OPV

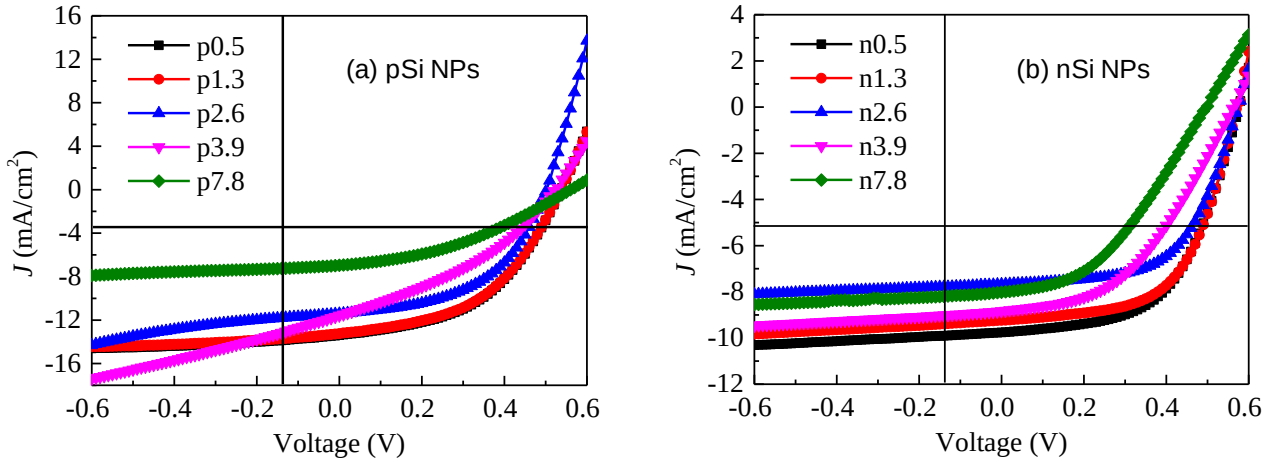

Fig. 7. *J-V* curves of devices incorporated with various concentrations of a) pSi NPs and b) nSi NPs

devices.

In pSi NPs incorporated devices, the J_{SC} increases for p0.5, p1.3 and then slowly comes down for p2.6 and p3.6 (Fig. 8a). However, the mean J_{SC} values for all the pSi NPs incorporated devices lie above that of reference device. Reason for J_{SC} improvement is seen in previous section. Variation of PCE, follows the trend of J_{SC} (Fig. 8b). Open-circuit voltage (V_{OC}) remains constant for all the blends (Fig. 8c). Nevertheless, fill-factor (FF) reduces by half (Fig. 8d), when the concentration increases from Ref, p0.5, to p7.8, leading to decrease in PCE even when J_{SC} is high. FF decrement is due to the appearance of S-shaped curves in devices with high concentration of pSi NPs (Fig. 7).

In nSi devices, J_{SC} increases slightly for n0.5 and n1.3 and falls off for n2.6, n3.9 and n7.8 (Fig. 9a). PCE follows the trend of J_{SC} and a maximum of 3.13% is observed in this case (Fig. 9b). This can be seen from the poor PL quenching efficiency by the nSi NPs, as discussed in Fig. 6b. V_{OC} remains constant for these devices also (Fig. 9c). Unlike pSi devices, where the FF decreases drastically on addition of NPs, in case of nSi devices, FF remains constant for low concentration devices and decreases drastically for n3.9 and n7.8 (Fig. 9d).

Decrease in FF for high concentration devices (in both pSi and nSi), can be due to the increase in the roughness of the devices leading to mismatch between electrode and active material. pSi devices experienced reduction in FF, even at low concentration. However, FF of nSi low concentration devices

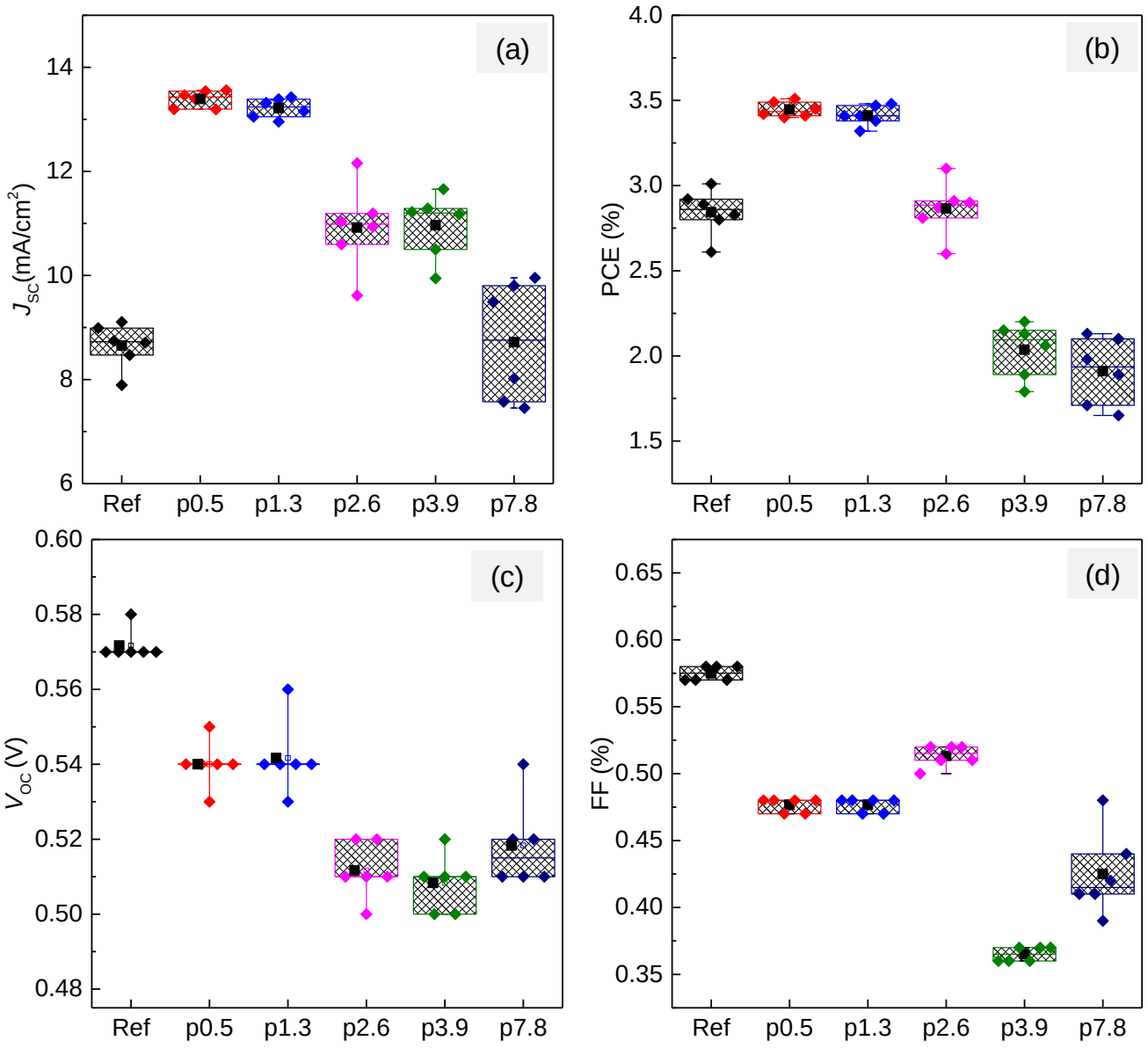

Fig. 8. Device parameters for pSi NPs incorporated devices. a) J_{SC}, b) PCE, c) V_{OC} and d) FF. X-axis represents the devices with different concentrations of pSi NPs and the reference device.

remains unvaried.

In pSi devices, the P3HT/NP interface can aid in exciton dissociation due to the optimum energy level difference ($CB_{(P3HT)} - CB_{Si}$ = 1.15eV). During the exciton dissociation, electrons will move to the conduction band edge of pSi NPs. These NPs are electron deficient and hence the dissociated electrons can be trapped by pSi particles. This reduces the FF in pSi devices.

In case of P3HT/nSi NP interface, when the exciton dissociates, electrons will go to the conduction band edge of nSi NPs. these NPs are rich in electrons and the electron from dissociation can float to cathode at ease. This phenomenon explains the constant FF for devices – n0.5, n1.3 and n2.6.

Interface for exciton dissociation is provided by the donor/NP surface. However, the interpenetrating network for the charge carrier transport will not be smooth as the particles will be randomly arranged. In certain cases such as the use of nanowires and nanorods which are highly oriented can help in reducing the effect of providing random pathways for charge transport (Finck and Schwartz, 2013; Wright and Uddin, 2012). In this study, the NPs used are obtained from the milling and the particles are of irregular shape (Fig. 1b). Hence the increase in NP concentration can result in reducing the dominantly active interface between P3HT and $PC_{61}BM$ by hindering the charge transport due to shape factor. This in turn leads to recombination of the dissociated excitons (Alsari et al., 2015). This can also be expected due to recombination arising from the imbalanced charge extraction primarily due to difference in charge carrier mobility between active material with and without NPs (Sun et al., 2016; Tremolet de Villers et al., 2009). In accordance, the hole mobility of P3HT reduces due to the addition of pSi NPs, as can be seen from Fig. S1. The morphology of the active layers with nano-sized grains is seen in the Fig. S2 for different concentrations of the NPs. The devices show no significant change in the domain size and hence the contribution of this factor in efficiency variation can be minimal. EQE spectra of the devices are shown in Fig. S3 and the device parameters are given in Table S1. Improved current collection is observed throughout the wavelength range, in case of pSi devices. This can be due to the improved current collection as discussed earlier. EQE values of the nSi devices are poor when compared to that of pSi devices.

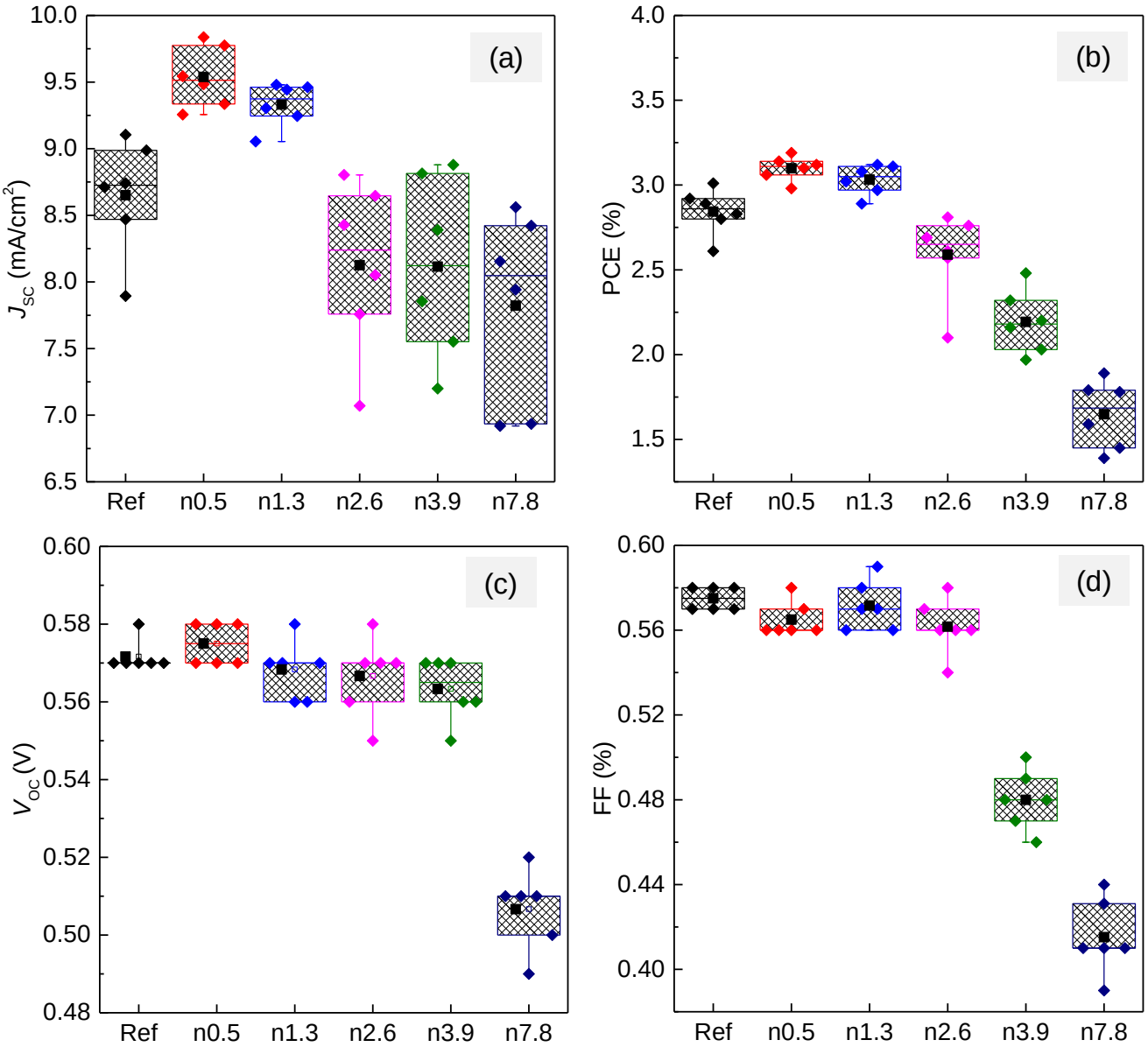

Fig. 9. Device parameters for nSi NPs incorporated devices. a) J_{SC}, b) PCE, c) V_{OC} and d) FF. X-axis represents the devices with different concentrations of nSi NPs and the reference device.

Conclusions

In conclusion, it is observed that the addition of doped silicon nanoparticles in the P3HT:$PC_{61}BM$ solar cells has effectively improved the device efficiency. The PCE enhancement is seen as a reflection of increased current collection aided by the cascading energy levels of due to the added silicon NP. Utilising the n-type and p-type NP dopants resulted in shift of fermi levels. In p-type silicon nanoparticles the fermi energy level was well aligned with the band structure of the base P3HT:$PC_{61}BM$ device resulting improved charge collection leading higher J_{SC} and overall efficiency of about 3.46% which translates to more than 21% as compared to reference device. Moreover, n-type Si nanoparticle has shown an efficiency increment of about 10%. Hence, the addition of nanoparticle has to be designed by tuning the energy levels which can be achieved by doping and mixing with optimized weight ratios in addition to reducing the size of NPs.

Acknowledgement

Authors gratefully acknowledge the financial support from Department of Science and Technology, Government of India (DSTO 1286). This work is supported by part under the US– India Partnership to Advance Clean Energy-Research (PACE-R) for the Solar Energy Research Institute for India and the United States (SERIIUS), funded jointly by the U.S. Department of Energy (Office of Science, Office of Basic Energy Sciences, and Energy Efficiency and Renewable Energy, Solar Energy Technology Program, under Subcontract DE-AC36-08GO28308 to the National Renewable Energy Laboratory, Golden, Colorado) and the Government of India, through the Department of Science and Technology under Subcontract IUSSTF/JCERDC-SERIIUS/ 2012 dated 22nd Nov. 2012. Authors also thank the microscopic facilities provided by AFMM center and CeNSE at Indian Institute of Science. Authors would like to thank useful discussions with Prof. N. Ravishankar of Materials Research Centre, IISc. Authors are also grateful to the help from Mr. Himanshu of ICER, IISc in carrying out the experiments.

References

A. Dowland, S., X. Reynolds, L., MacLachlan, A., B. Cappel, U., A. Haque, S., 2013. Photoinduced electron and hole transfer in CdS:P3HT nanocomposite films: effect of nanomorphology on charge separation yield and solar cell performance. Journal of Materials Chemistry A 1, 13896-13901.

Alsari, M., Omar, Y.M., Panda, M.K., Chiesa, M., Naumov, P., Lilliu, S., 2015. Detrimental Effect of Silicon Nanoparticles on P3HT:PCBM-Based OPV Devices. Macromolecular Chemistry and Physics 216, 1155-1160.

Arici, E., Sariciftci, N.s., Meissner, D., 2003. Hybrid Solar Cells Based on Nanoparticles of $CuInS_2$ in Organic Matrices. Advanced Functional Materials 13, 165-171.

Barai, K., Tiwary, C.S., Chattopadhyay, P.P., Chattopadhyay, K., 2012. Synthesis of free standing nanocrystalline Cu by ball milling at cryogenic temperature. Materials Science and Engineering: A 558, 52-58.
Baranovskii, S.D., Wiemer, M., Nenashev, A.V., Jansson, F., Gebhard, F., 2012. Calculating the Efficiency of Exciton Dissociation at the Interface between a Conjugated Polymer and an Electron Acceptor. The Journal of Physical Chemistry Letters 3(9), 1214-1221.
Cheng, F., Fang, G.J., Fan, X., Liu, N.S., Sun, N.H., Qin, P.L., Zheng, Q., Wan, J.W., Zhao, X.Z., 2011. Enhancing the short-circuit current and efficiency of organic solar cells using MoO_3 and CuPc as buffer layers. Solar Energy Materials and Solar Cells 95(10), 2914-2919.
Chi, D., Qu, S., Wang, Z., Wang, J., 2014. High efficiency P3HT:PCBM solar cells with an inserted PCBM layer. Journal of Materials Chemistry C 2(22), 4383-4387.
Dang, M.T., Hirsch, L., Wantz, G., 2011. P3HT:PCBM, best seller in polymer photovoltaic research. Adv Mater 23(31), 3597-3602.
Dayal, S., Reese, M.O., Ferguson, A.J., Ginley, D.S., Rumbles, G., Kopidakis, N., 2010. The Effect of Nanoparticle Shape on the Photocarrier Dynamics and Photovoltaic Device Performance of Poly(3-hexylthiophene):CdSe Nanoparticle Bulk Heterojunction Solar Cells. Advanced Functional Materials 20, 2629-2635.
Finck, B.Y., Schwartz, B.J., 2013. Understanding the origin of the S-curve in conjugated polymer/fullerene photovoltaics from drift-diffusion simulations. Appl Phys Lett 103(5), 053306.
Gur, I., Fromer, N.A., Alivisatos, A.P., 2006. Controlled Assembly of Hybrid Bulk−Heterojunction Solar Cells by Sequential Deposition. The Journal of Physical Chemistry B 110, 25543-25546.
Hames, Y., Alpaslan, Z., Kösemen, A., San, S.E., Yerli, Y., 2010. Electrochemically grown ZnO nanorods for hybrid solar cell applications. Solar Energy 84(3), 426-431.
Jaramillo, J., Boudouris, B.W., Barrero, C.A., Jaramillo, F., 2015. Design of Super-Paramagnetic Core–Shell Nanoparticles for Enhanced Performance of Inverted Polymer Solar Cells. ACS Applied Materials & Interfaces 7, 25061-25068.
Kubelka, P., 1948. New Contributions to the Optics of Intensely Light-Scattering Materials. Part I. JOSA 38, 448-457.
Kudo, N., Shimazaki, Y., Ohkita, H., Ohoka, M., Ito, S., 2007. Organic–inorganic hybrid solar cells based on conducting polymer and SnO_2 nanoparticles chemically modified with a fullerene derivative. Solar Energy Materials and Solar Cells 91, 1243-1247.
Kundu, S., Varma, K.B.R., 2013. Synthesis, structural and optical properties of nanocrystalline $Ba_2NaNb_5O_{15}$. Crystengcomm 15, 8887-8893.
Kuo, C.Y., Tang, W.C., Gau, C., Guo, T.F., Jeng, D.Z., 2008. Ordered bulk heterojunction solar cells with vertically aligned TiO_2 nanorods embedded in a conjugated polymer. Appl Phys Lett 93, 033307.
Lee, W., Shin, S., Han, S.-H., Cho, B.W., 2008. Manipulating interfaces in a hybrid solar cell by in situ photosensitizer polymerization and sequential hydrophilicity/hydrophobicity control for enhanced conversion efficiency. Appl Phys Lett 92, 193307.
Liu, C.-Y., Holman, Z.C., Kortshagen, U.R., 2009. Hybrid Solar Cells from P3HT and Silicon Nanocrystals. Nano Lett 9, 449-452.
Liu, C.-Y., Holman, Z.C., Kortshagen, U.R., 2010. Optimization of Si NC/P3HT Hybrid Solar Cells. Advanced Functional Materials 20, 2157-2164.
MacLachlan, A.J., Rath, T., Cappel, U.B., Dowland, S.A., Amenitsch, H., Knall, A.-C., Buchmaier, C., Trimmel, G., Nelson, J., Haque, S.A., 2015. Polymer/Nanocrystal Hybrid Solar Cells: Influence of Molecular Precursor Design on Film Nanomorphology, Charge Generation and Device Performance. Advanced Functional Materials 25, 409-420.

Naoto, S., Tsuyoshi, H., Yoshio, S., Tohru, T., 2010. Size- Tunable UV- Luminescent Silicon Nanocrystals. Small 6(8), 915-921.
Narayan, M.R., Singh, J., 2014. Exciton dissociation and design optimization in hybrid organic solar cells, 2014 Conference on Optoelectronic and Microelectronic Materials & Devices. pp. 262-265.
Pfadler, T., Coric, M., Palumbiny, C.M., Jakowetz, A.C., Strunk, K.-P., Dorman, J.A., Ehrenreich, P., Wang, C., Hexemer, A., Png, R.-Q., Ho, P.K.H., Müller-Buschbaum, P., Weickert, J., Schmidt-Mende, L., 2014. Influence of Interfacial Area on Exciton Separation and Polaron Recombination in Nanostructured Bilayer All-Polymer Solar Cells. ACS Nano 8, 12397-12409.
Streetman, B., Banerjee, S., 2015. Solid State Electronic Devices, Global Edition. Pearson Education Limited.
Sun, L., Sun, J.-X., Xiong, C.-H., Shi, X.-H., 2016. Trap-assisted recombination in disordered organic semiconductors extended by considering density dependent mobility. Solar Energy 135, 308-316.
Takanezawa, K., Tajima, K., Hashimoto, K., 2008. Efficiency enhancement of polymer photovoltaic devices hybridized with ZnO nanorod arrays by the introduction of a vanadium oxide buffer layer. Appl Phys Lett 93, 063308.
Tan, Z., Zhu, T., Thein, M., Gao, S., Cheng, A., Zhang, F., Zhang, C., Su, H., Wang, J., Henderson, R., Hahm, J.-i., Yang, Y., Xu, J., 2009. Integration of planar and bulk heterojunctions in polymer/nanocrystal hybrid photovoltaic cells. Appl Phys Lett 95, 063510.
Tauc, J., 1968. Optical properties and electronic structure of amorphous Ge and Si. Mater Res Bull 3, 37-46.
Tremolet de Villers, B., Tassone, C.J., Tolbert, S.H., Schwartz, B.J., 2009. Improving the Reproducibility of P3HT:PCBM Solar Cells by Controlling the PCBM/Cathode Interface. The Journal of Physical Chemistry C 113(44), 18978-18982.
Tsang, S.W., Fu, H., Wang, R., Lu, J., Yu, K., Tao, Y., 2009. Highly efficient cross-linked PbS nanocrystal/C60 hybrid heterojunction photovoltaic cells. Appl Phys Lett 95, 183505.
Venkataprasad Bhat, S., Govindaraj, A., Rao, C.N.R., 2011. Hybrid solar cell based on P3HT–ZnO nanoparticle blend in the inverted device configuration. Solar Energy Materials and Solar Cells 95, 2318-2321.
Wang, L., Liu, Y., Jiang, X., Qin, D., Cao, Y., 2007. Enhancement of Photovoltaic Characteristics Using a Suitable Solvent in Hybrid Polymer/Multiarmed CdS Nanorods Solar Cells. The Journal of Physical Chemistry C 111, 9538-9542.
Wilcoxon, J.P., Samara, G.A., Provencio, P.N., 1999. Optical and electronic properties of Si nanoclusters synthesized in inverse micelles. Phys Rev B 60(4), 2704-2714.
Wright, M., Uddin, A., 2012. Organic—inorganic hybrid solar cells: A comparative review. Solar Energy Materials and Solar Cells 107, 87-111.
Yang, J., Tang, A., Zhou, R., Xue, J., 2011. Effects of nanocrystal size and device aging on performance of hybrid poly(3-hexylthiophene):CdSe nanocrystal solar cells. Solar Energy Materials and Solar Cells 95, 476-482.
Yang, Y.M., Chen, W., Dou, L., Chang, W.-H., Duan, H.-S., Bob, B., Li, G., Yang, Y., 2015. High-performance multiple-donor bulk heterojunction solar cells. Nature Photonics 9, 190-198.
Yin, Z., Wei, J., Zheng, Q., 2016. Interfacial Materials for Organic Solar Cells: Recent Advances and Perspectives. Advanced Science 3, 1500362.
Yu, G., Gao, J., Hummelen, J.C., Wudl, F., Heeger, A.J., 1995. Polymer Photovoltaic Cells: Enhanced Efficiencies via a Network of Internal Donor-Acceptor Heterojunctions. Science 270, 1789-1791.
Zhao, S., Pi, X., Mercier, C., Yuan, Z., Sun, B., Yang, D., 2016. Silicon-nanocrystal-incorporated ternary hybrid solar cells. Nano Energy 26, 305-312.
Zhou, Y., Eck, M., Krüger, M., 2010. Bulk-heterojunction hybrid solar cells based on colloidal nanocrystals and conjugated polymers. Energ Environ Sci 3, 1851-1864.

Zhou, Y., Eck, M., Men, C., Rauscher, F., Niyamakom, P., Yilmaz, S., Dumsch, I., Allard, S., Scherf, U., Krüger, M., 2011a. Efficient polymer nanocrystal hybrid solar cells by improved nanocrystal composition. Solar Energy Materials and Solar Cells 95, 3227-3232.
Zhou, Y., Eck, M., Veit, C., Zimmermann, B., Rauscher, F., Niyamakom, P., Yilmaz, S., Dumsch, I., Allard, S., Scherf, U., Krüger, M., 2011b. Efficiency enhancement for bulk-heterojunction hybrid solar cells based on acid treated CdSe quantum dots and low bandgap polymer PCPDTBT. Solar Energy Materials and Solar Cells 95(4), 1232-1237.
Zhu, X., Choy, W.C.H., Xie, F., Duan, C., Wang, C., He, W., Huang, F., Cao, Y., 2012. A study of optical properties enhancement in low-bandgap polymer solar cells with embedded PEDOT:PSS gratings. Solar Energy Materials and Solar Cells 99, 327-332.
Zhu, X.Y., Yang, Q., Muntwiler, M., 2009. Charge-Transfer Excitons at Organic Semiconductor Surfaces and Interfaces. Accounts of Chemical Research 42(11), 1779-1787.

Highlights

- Adding doped Si nanoparticles in P3HT:$PC_{61}BM$ solar cells improves device efficiency
- Fermi levels of Si, aligning with P3HT and $PC_{61}BM$ enhances current collection
- 35% improvement in J_{sc} due to p-type Si NP addition
- Minimal concentration of Si nanoparticle resulted in maximum efficiency
- Other than particle size reduction, band aligning can also be performed by doping

Graphical abstract